Self-Assembly of Four-Layer Woodpile Structure from Zigzag ABC Copolymer/Aluminosilicate Concertinas

Gilman E. S. Toombes,[†,○] Surbhi Mahajan,[‡,⊥] Matthew Weyland,[§,#] Anurag Jain,[‡,&] Phong Du,[‡,⊥] Marleen Kamperman,[‡] Sol M. Gruner,[†,∥] David A. Muller,[§] and Ulrich Wiesner*[,‡]

Departments of Physics, Materials Science and Engineering, and Applied and Engineering Physics, Cornell University, Ithaca, New York 14853, and Cornell High Energy Synchrotron Source (CHESS)

Received May 2, 2007; Revised Manuscript Received September 10, 2007

ABSTRACT: Scanning transmission electron tomography was used to determine the three-dimensional structure of a poly(ethylene-*alt*-propylene-*block*-ethylene oxide-*block*-*n*-hexyl methacrylate) (PEP-*b*-PEO-*b*-PHMA) triblock copolymer/aluminosilicate material with domain volume fractions of $f_{PEP} = 0.19$, $f_{PEO+aluminosilicate} = 0.32$, and $f_{PHMA} = 0.49$. The PEO/aluminosilicate domains formed layers of zigzag-shaped strands (concertinas). Strands were arranged in a four-layer woodpile structure (Sozuer, H. S.; Dowling, J. P. *J. Mod. Opt.* **1994**, *41*, 231−239),[1] in which strands in successive layers run in alternate directions (∼75°) and the third and fourth layers are offset. Modeling suggests the PEP and PHMA domains on the outside of each PEO/aluminosilicate strand may stabilize this unusual structure. This result suggests that synthetic macromolecules with multidomain architectures, such as ABC triblock copolymers, can direct the assembly of silica and other ceramic materials into complex new morphologies.

Introduction

In biosilicification, multidomain proteins direct the assembly of silica−organic composites[2−4] into complex, hierarchical structures with outstanding materials properties.[5,6] Mimicking aspects of this organic−inorganic self-assembly process is of great interest for applications including catalysts, selective membranes, and optical materials.[7−13] The length scale of phase separation in block copolymers is ideal for this purpose, and synthetic macromolecules with AB or ABA block architectures have been used to direct silica-type materials into ordered structures with lamellar, hexagonal, or cubic symmetry.[14−17] However, a wide gulf remains between these synthetic composites and the complex structure of biological silica.

Bridging this divide will require the use of structure-directing organic molecules with more complex interactions and phase behavior. The introduction of a third block in ABC triblock copolymers leads to a diverse range of complex morphologies.[18−20] Using ABC block copolymers as structure-directing agents promises numerous benefits, including easier access to continuous network structures,[21] novel helical[22] and noncentrosymmetric[23] structures, and the possibility of independently structuring two or more types of inorganic material. To date, however, using the rich assembly behavior of ABC block copolymers to mesostructure silica remains a challenge.

In this report we describe a new amorphous aluminosilicate mesostructure formed with the amphiphilic ABC triblock copolymer, poly(ethylene-*alt*-propylene-*block*-ethylene oxide-*block*-*n*-hexyl methacrylate) (PEP-*b*-PEO-*b*-PHMA).[24] The aluminosilicate precursors partition into the hydrophilic PEO middle block of the copolymer,[25] while the low glass transition temperature of all three blocks (T_g(PEP) ≈ −62 °C, T_g(PEO) ≈ −60 °C, T_g(PHMA) ≈ −5 °C) facilitates the formation of well-ordered mesostructures. PEO crystallization, T_m(PEO) ≈ 50 °C, is suppressed in the presence of the nanometer-sized aluminosilicate particles. While a range of compositions has been studied,[26] here we discuss only results for an ABC copolymer/aluminosilicate hybrid with domain volume fractions of $f_{PEP} = 0.19$, $f_{PEO+aluminosilicate} = 0.32$, and $f_{PHMA} = 0.49$.

Three-dimensional imaging of the material using scanning transmission electron tomography[27] revealed a complex morphology not previously achieved using AB or ABA block copolymers. The PEO/aluminosilicate domains formed layers of zigzag-shaped strands with wiggles like the bellows of a concertina. Remarkably, strands in successive layers of the material ran in alternating directions leading to a four-layer woodpile lattice.[1,28] Structural modeling suggests this unusual stacking may result from the presence of both PEP and PHMA domains on the outside of each aluminosilicate strand.

These results demonstrate that, in analogy to the multidomain proteins in biosilicification, triblock copolymers can direct the assembly of silica into complex structures. Furthermore, combining complex ABC copolymer architectures with the physical, electrical, and optical properties of inorganic materials holds considerable promise for functional materials.[29]

Experimental Methods

Materials Synthesis. Poly(ethylene-*alt*-propylene-*block*-ethylene oxide-*block*-*n*-hexyl methacrylate) (PEP-*b*-PEO-*b*-PHMA) was synthesized via stepwise anionic polymerization, catalytic hydrogenation, and atom transfer radical polymerization as described earlier.[24] The molecular weight (M_n = 25 100 g/mol) and polydispersity (M_w/M_n = 1.08) were determined via NMR and GPC.[24] From the room-temperature densities of the corresponding homopolymers,[30−32] block volume fractions for the copolymer were $f_{PEP} = 0.22$, $f_{PEO} = 0.20$, and $f_{PHMA} = 0.58$. To prepare the hybrid

* Corresponding author: E-mail: ubw1@cornell.edu.
† Department of Physics, Cornell University.
‡ Department of Materials Science and Engineering, Cornell University.
§ Department of Applied and Engineering Physics, Cornell University.
∥ Cornell High Energy Synchrotron Source.
⊥ Present address: DuPont Central Research and Development, Experimental Station, Rt141 and Henry Clay, Wilmington, DE 19880-0328.
Present address: Monash Centre for Electron Microscopy, Bldg 81, Monash University, VIC 3800, Australia.
& Present address: Intel Corporation, 5200 NE Elam Young Parkway RA3-355, Hillsboro, OR 97124.
○ Present address: PCC UMR168, Institut Curie, 11 rue Pierre et Marie Curie, Paris 75005, France.

10.1021/ma071004s CCC: $40.75
Published on Web 01/16/2008

material, the ABC triblock copolymer was dissolved in a 50−50 mixture (by volume) of tetrahydrofuran and chloroform to form a 2 wt % solution. The tetrahydrofuran/chloroform solvent mixture was selected because the copolymer and aluminosilicate sol are both quite soluble in it and because in prior work with PI-*b*-PEO diblock copolymer/aluminosilicate materials,[17,25] the rate of evaporation of the tetrahydrofuran/chloroform mixture proved suitable for forming well-ordered copolymer/inorganic structures. In a second vial, a sol of 3-(glycidyloxypropyl)trimethoxysilane (GLYMO) and aluminum *sec*-butoxide (mole ratio of 8:2) was prepared following a two-step acid-catalyzed hydrolysis procedure described previously.[17] The aluminosilicate sol was added to the ABC triblock copolymer solution (copolymer:sol weight ratio of 64:36), and the resulting solution was stirred for 1 h at a temperature of 25 °C. This solution was then transferred to glass evaporation dishes and films of the copolymer/alumininosilicate material cast by evaporation on a hot plate at 50 °C. The resultant solid, clear film (∼0.5 mm thick) was annealed for 1 h in a vacuum oven (130 °C) to remove residual solvent. After accounting for the evaporation of volatile hydrolysis products[17] and assuming a density of 1.4 g/cm^3 for the PEO + inorganic phase,[25] the domain volume fractions of the hybrid material were $f_{PEP} = 0.19$, $f_{PEO+aluminosilicate} = 0.32$, and $f_{PHMA} = 0.49$.

X-ray Scattering. Small- and wide-angle X-ray scattering data were gathered using a laboratory source. Briefly, Cu Kα X-rays ($\lambda = 0.154$ nm) were generated with a Rigaku RU-3HR generator (tube voltage = 42 kV, tube current = 56 mA, 2 mm × 0.2 mm point focus on a copper anode), filtered by a nickel foil (thickness = 10 μm; Goodfellow, PA), and focused and further monochromatized with a pair of Franks mirrors.[33] The flux at the sample was ∼4 × 10^7 X-ray photons s^{-1} in a 1 mm × 1 mm diameter beam. Small-angle X-ray scattering (SAXS) data were gathered using a 60 or 80 cm flight tube while wide-angle X-ray scattering (WAXS) was measured using a 1.5 cm flight tube. At the end of the flight tube, the transmitted X-ray beam was blocked with a small (typical diameter of 2−3 mm) circle of lead tape while the scattered X-rays were imaged with a home-built 2-D X-ray area detector consisting of a phosphor screen, fiber-optic coupler, and 1024 × 1024 pixel CCD.[34] The distance from the sample to detector and position of the beam center were determined using silver behenate ($d_{lamellar} = 5.8376$ nm)[35] and silver stearate ($d_{lamellar} = 4.868$ nm)[36] calibrants. Samples of the ABC copolymer were placed in glass X-ray capillaries ($d = 1$ mm, Charles Supper, MA) and annealed in a vacuum (150 °C for 2 h) before data collection. Samples of the hybrid material were cut to size (1 mm wide by 5 mm thick) and positioned using a mechanical rotation stage. For unoriented samples, X-ray scattering was azimuthally averaged about the incident beam direction and reported as a function of the magnitude of the scattering vector, $s = 2\sin(\theta)/\lambda$, where 2θ is the angle between incident and scattered radiation.

TEM. Thin sections (50−100 nm thickness) of the hybrid material were cut at 210 K using a Leica Ultracut UCT microtome and transferred to copper TEM grids. To isolate individual strands, the hybrid material was dispersed in toluene overnight (1 mg hybrid/1 g toluene) and the solution then sonicated briefly. Approximately 10 μL of this solution was evaporated onto a holey carbon film supported on a 200 mesh copper TEM grid. Dark-field energy-filtered transmission electron microscopy was performed using a LEO 922 Omega EF-TEM (tungsten filament) microscope at 200 kV and objective aperture angle of 3.6 mrad. Using a slow-scan CCD (2K × 2K), images were acquired for inelastic scattering at the silicon L-edge (120−145 eV). These imaging conditions provided contrast for the aluminosilicate both through its silicon content and higher average atomic number relative to the ABC copolymer.

STEM Tomography. All tomography was carried out using an FEI Tecnai F20-ST field emission gun scanning transmission electron microscope (FEG-(S)TEM). The STEM probe size, and nominal resolution, at the used settings is ∼1.6 Å. Images were acquired using a Fischione high-angle annular dark field (HAADF) detector with the detector inner radius setting of ∼30 mrad. By collecting electrons scattered to high angles in all scattering directions, HAADF STEM is sensitive to the scattering from the average atomic number and projected thickness of the specimen. As the aluminosilicate has a higher average atomic number than the organic material, it evidences a higher average scattering and a higher intensity in HAADF STEM images. Tilt series were acquired automatically using FEI Xplore3D tomography acquisition software. The tilt series of the isolated strand specimen was acquired from ±72° with a 2° increment, a total of 73 images, at a magnification of 320 000×, corresponding to a pixel size of 0.35 nm in a 1024 × 1024 pixel image. The tilt series of the bulk specimen was acquired from ±72° with a 2° increment, a total of 73 images, at a magnification of 115 000×, corresponding to a pixel size of 0.99 nm in a 1024 × 1024 pixel image. Because of the limited tilt range, imposed by the need to clamp the specimen in the holder, the resolution in tomographic reconstructions is inhomogeneous: the resolution is highest in *x*, along the tilt axis, intermediate along *y*, perpendicular to the tilt axis, and lowest in *z*, depth direction.

Tomographic Reconstruction. Tomographic data processing was performed using custom software[27] designed in IDL (Interactive Data Language) V6.0. Alignment of tilt series, to a common tilt axis, was achieved by sequential cross-correlation and manual adjustment. Tomographic reconstruction of the bulk series was carried out by *r*-weighted back-projection,[37] while the strand series was reconstructed by simultaneous iterative reconstruction[38] (SIRT), in a multiplicative mode with 30 iterations.

Three-Dimensional Visualization. All three-dimensional visualizations of both strand and bulk reconstructions were carried out using Amira V3. Surface renders were generated using an isosurface value at the measured surface intensity of the aluminosilicate in the reconstruction. There is a small error in this value due to the nonhomogeneity of the reconstruction intensity in the three volume directions. Voxel projections of the bulk specimens were generated using modified optical absorption values in order to mask the effect of the high-intensity contaminants and highlight the aluminosilicate structure.

Structural Modeling. Block domains were modeled in MATLAB using level set functions[39] consistent with the lattice symmetry and dimensions determined from the STEM tomographic reconstruction. For the PEO/ aluminosilicate domains, Fourier coefficients were matched to the volume fraction and structure of the isolated strand reconstruction. Functions for the distance to the nearest strand and next nearest strand were used to generate level sets for the generalized Voronoi cell as well as the PEP and PHMA domains.

Results

ABC Copolymer Structure. The Flory−Huggins interaction parameters for this PEP-*b*-PEO-*b*-PHMA copolymer are approximately $\chi_{AB}N = 180$, $\chi_{BC}N = 70$, and $\chi_{AC}N = 25$ as estimated using the approximation of Hildebrand and Scott[40]

$$\chi_{ij} = \frac{V_{ref}(\delta_i - \delta_j)^2}{RT}$$

where V_{ref} is the segment reference volume and δ_i the Hildebrand solubility parameter for polymer *i* ($^{41}\delta_{PEP} = 16.0$ (MPa)$^{1/2}$, $^{42}\delta_{PEO} = 20.2$ (MPa)$^{1/2}$, and $^{42}\delta_{PHMA} = 17.6$ (MPa)$^{1/2}$). The relatively small mixing enthalpy of the A and C blocks ($\chi_{AC}N < \chi_{AB}N$, and $\chi_{BC}N$) favors optional AC domain interfaces over the obligatory AB and BC interfaces. Theoretical[20] and experimental[43] studies in this regime reported structures with a cylindrical A/B core surrounded by the outer C block for block volume fractions corresponding to this ABC copolymer ($f_A \approx f_B \approx 0.2 < f_C \approx 0.6$). Within the cylindrical A/B core, several B-domain structures have been observed, including a cylindrical shell, perforated cylinder, cylindrical rods, helical rods, and cylindrical rings.[22,43]

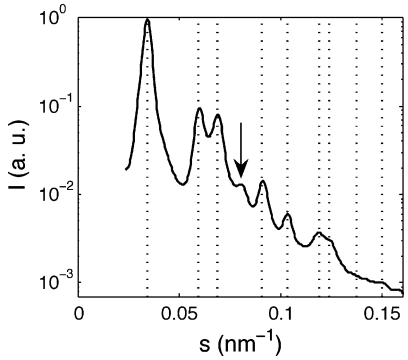

Figure 1. SAXS from the parent ABC block copolymer at 100 °C. The vertical dotted lines indicate the allowed reflections for a hexagonal unit cell (repeat spacing 29.08 ± 0.15 nm). The peak at $s = (8.06 \pm 0.05) \times 10^{-2}$ nm^{-1} (arrow) does not index to this hexagonal lattice.

Long-range ordering within the parent ABC copolymer is evident from the SAXS data shown in Figure 1. All but one of the peaks could be indexed to the first seven reflections of a hexagonal lattice (repeat spacing of 29.08 ± 0.15 nm), while the additional peak at $s = (8.06 \pm 0.05) \times 10^{-2}$ nm^{-1} (12.4 ± 0.1 nm *d*-spacing) requires the structure to have a third crystallographic axis. Unfortunately, transmission electron microscopy of the ABC copolymer was challenging. Because the glass temperature of all three blocks is below room temperature, samples must be both microtomed and imaged at cryogenic temperatures, and a cryo-EM stage was not available. Furthermore, PEP-*b*-PEO-*b*-PHMA cannot readily be stained with RuO_4 or OsO_4, and contrast between the unstained blocks is low. Although the SAXS data are consistent with the anticipated structure of cylindrical A/B domains arranged in a hexagonal array, additional information is needed to determine the actual structure of the ABC copolymer.

Hybrid Structure. Because the aluminosilicate particles are highly compatible with the PEO block[25] and relative incompatible with the PEP and PHMA blocks, the hybrid material should contain distinct PEO−aluminosilicate domains. These PEO−aluminosilicate domains have a greater volume fraction (parent copolymer $f_{PEO} = 0.20 \rightarrow$ hybrid material $f_{PEO+aluminosilicate} = 0.32$) and incompatibility with the PEP and PHMA blocks than the PEO block in the parent ABC copolymer. Thus, even though the ABC copolymer directs the assembly of the aluminosilicate particles, the morphology of the resulting hybrid material is not expected to match that of the parent ABC copolymer.[67] 2-D SAXS from the hybrid material is shown in Figure 2a. The sample was oriented so that the normal to the film surface was directed along the vertical (*y*-axis). The elongation of the main diffraction ring along the film normal (vertical) reflects a modest, unidirectional shrinkage ($\epsilon = 9\% \pm 1.5\%$) common for solvent-cast materials.[44] Rotating the sample about the film normal (vertical; *y*-axis) left the distinct diffraction spots in Figure 2a unaltered, indicating a partial fiber-type orientation[45] of the structure. The four Bragg spots on the main ring ($|s_x| = 0.047 \pm 0.001$ nm^{-1}, $|s_y| = 0.020 \pm 0.002$ nm^{-1}, 23.0 ± 2.5° from horizontal) have the largest integrated scattering intensity when the fiber alignment is accounted for. Figure 2b shows the pseudo-fiber average for the sample computed using the expression

$$I_{AVG}(s) = \int_{\varphi=0}^{\varphi=2\pi} I\left(s \sin \varphi, \frac{s \cos \varphi}{1-\epsilon}\right) \frac{|\sin \varphi| \, d\varphi}{4}$$

where $I(s_x,s_y)$ is the 2-D scattering intensity and ϵ is the unidirectional shrinkage of the sample along the film normal.

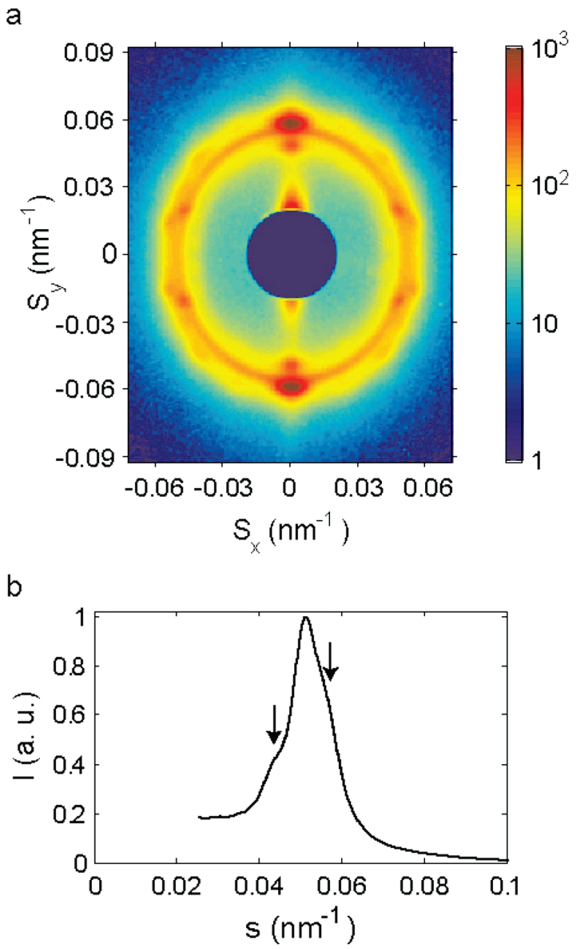

Figure 2. 2-D SAXS pattern (logarithmic scale) from the hybrid material (a). The sample was oriented so the normal to the film surface was directed vertically (*y*-axis). The majority of scattering is unoriented although the Bragg spots indicate some fiber-type alignment along the normal to the film surface (vertical). The main ring has a repeat spacing of 19.4 ± 0.5 nm and is slightly elliptical (9% ± 1.5%) because of anisotropic shrinkage along the surface normal. Fiber-averaged integrated scattering intensity SAXS pattern from the hybrid material (b). In addition to the main peak at 19.4 ± 0.5 nm ($s = (5.15 \pm 0.13) \times 10^{-2}$ nm^{-1}), arrows mark the shoulders evident at repeat spacings of 22.8 ± 0.5 nm ($s = (4.39 \pm 0.09) \times 10^{-2}$ nm^{-1}) and 17.4 ± 0.5 nm ($s = (5.75 \pm 0.16) \times 10^{-2}$ nm^{-1}).

The center of the diffraction ring has a repeat spacing of 19.4 ± 0.5 nm with shoulders at 22.8 ± 0.5 and 17.4 ± 0.5 nm. The lack of a unique lattice orientation and/or higher-order reflections prevented a direct determination of the crystal lattice from SAXS data. However, the SAXS data clearly indicate the structure of the hybrid material is different from that of the parent ABC copolymer.

Thin sections (~60 nm) of the bulk material were examined via dark-field energy-filtered transmission electron microscopy. TEM micrographs were prepared from several different pieces of the hybrid material, and representative images are shown in Figure 3a,b. Figure 3a confirms the periodic character of the aluminosilicate (bright) structure but differs from projections of hexagonally packed cylinders. However, individual aluminosilicate domains isolated by solvent dispersal and sonication are clearly one-dimensional strands (Figure 3b) with a curious "zigzag" character. The projection in Figure 3a gives the appearance of layers of strands running in two almost perpendicular directions, but the detailed structure of the strands and their arrangement within the bulk material remain unclear from these TEM micrographs.

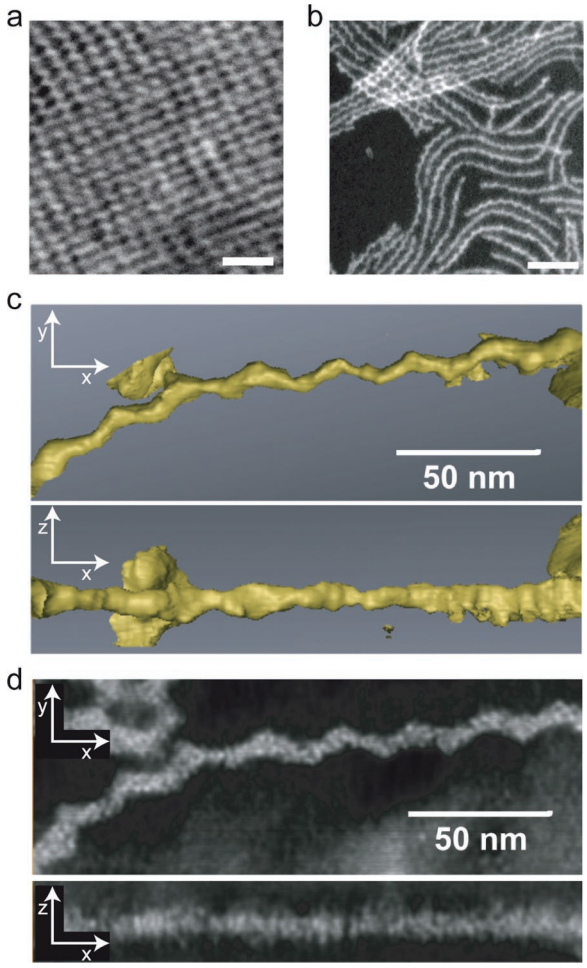

Figure 3. Electron microscopy of strand structure. Dark-field EF-TEM images of a thin section of the bulk material (aluminosilicate bright) (a, scale bar 100 nm) and individual aluminosilicate strands (b, scale bar 200 nm). A tomographic reconstruction of an individual hybrid strand was obtained from a tilt series of HAADF-STEM images. Isosurface renders showing the surface of the aluminosilicate strand viewed from the top and side exhibit a clear "concertina" structure (c and Supporting Information movie). The thickness of strands is ~10 nm, while the wiggles along each strand have a period of $d_w \sim$ 24 nm and a peak-to-peak amplitude of ~5 nm (c). Corresponding slices through the center of the reconstruction shows individual aluminosilicate particles (diameter ~ 2 nm) within the body of the concertina (d).

To resolve the ambiguity of SAXS and TEM micrographs, we applied electron tomography[46] in which a real-space three-dimensional reconstruction is determined using a tilt series of electron micrographs. While conventional bright field electron tomography is classically used for the examination of biological macromolecules, it has also been successfully applied to analyze the 3D morphology of block copolymer systems[47,48] and porous inorganic materials.[49] Recent adaptation of the technique to work with STEM imaging[27] has made it ideal for studying materials with differing atomic numbers and densities.

The tomographic reconstruction of an isolated strand (Figure 3c,d and Supporting Information movie) revealed a complex structure. In one direction, the individual aluminosilicate strands show a "zigzag" shape with a wiggle period of $d_w \approx 24$ nm and peak-to-peak wiggle amplitude of ~5 nm. In the perpendicular direction, the strands are almost flat, leading to an overall structure of a stretched "concertina". The cross section of the concertina is ~5 nm wide by 10 nm thick although variations are evident along its length.

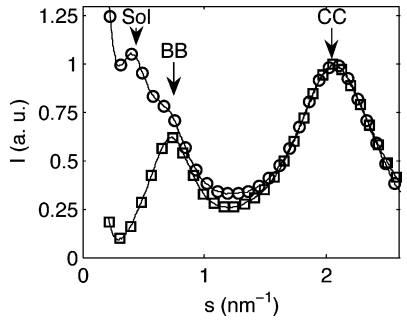

Figure 4. Wide-angle X-ray scattering data from the parent ABC copolymer (squares) and hybrid material (circles) show correlations between the aluminosilicate particles in the PEO−aluminosilicate domains ($d_{SOL} = 2.5 \pm 0.3$ nm), the polymer backbones within the PHMA domains ($d_{BB} = 1.35 \pm 0.03$ nm), and the alkyl chains ($d_{CC} = 0.48 \pm 0.01$ nm) in all three domains.

The resolution of the reconstruction is also sufficient to resolve the internal structure of the concertina. Sections through the reconstruction shown in Figure 3d reveal a distinctly bimodal distribution of intensity with bright and dark regions approximately 1−3 nm in size. The bright regions correspond to aluminosilicate particles (high atomic number, e.g., high *Z*) while the polymer-rich regions (low *Z*) are darker. This internal structure within the PEO−aluminosilicate domains is also evident in the wide-angle X-ray scattering data shown in Figure 4. WAXS from the parent ABC copolymer has two distinct peaks corresponding to the alkyl chain−chain distance ($d_{CC} = 0.48 \pm 0.01$ nm) and mean spacing between methacrylate backbones ($d_{BB} = 1.35 \pm 0.03$ nm) within the PHMA block.[50,51] For the hybrid material, a third peak is present arising from correlations between the densely packed aluminosilicate particles[25] within the PEO−aluminosilicate domain ($d_{SOL} = 2.5 \pm 0.3$ nm).

To determine the arrangement of individual concertinas, a tomographic reconstruction was performed upon a thin section of the bulk material, as shown in Figure 5. Strikingly, the unit cell consists of a four-layer woodpile[1,28] (Figure 6) in which the direction of concertinas in successive layers alternates. The first and third layers of concertinas are directed along the [110] diagonal while the second and fourth layers are run along the [1$\bar{1}$0] diagonal. Furthermore, layers are staggered with the third and fourth layers offset by $(\boldsymbol{a} + \boldsymbol{c})/2$.

For a projection along the [110] direction (Figures 5a and 6e), concertinas in the even layers are end on and appear as staggered rows of dots, while concertinas in the odd layers run horizontally across the projection. Rotating by ~75° to the [1$\bar{1}$0] direction (Figures 5b and 6f), the odd layers of the lattice are now end on and form a staggered dot pattern. The lack of homogeneity in the reconstruction resolution (Experimental Methods) may account for why the side-on layers are clearer in Figure 5a than Figure 5b. The alternating direction of concertinas is most evident in slices taken through consecutive layers in the sequence. In Figure 5c the strands run in alternate directions ($\boldsymbol{a} + \boldsymbol{b}$, $\boldsymbol{a} - \boldsymbol{b}$, $\boldsymbol{a} + \boldsymbol{b}$, ...) in successive layers. Within each layer the average distance between strands is $d_{ip} \approx 23.3$ nm while the distance between layers is ~11 nm. Because strands in successive layers cross at $\phi \approx 75°$, the maximum possible symmetry of the unit cell is the orthorhombic *Fddd* space group[52] (No. 70, IUCr) with lattice constants $|a| = 29.4 \pm 0.8$ nm, $|b| = 38.3 \pm 1.0$ nm, and $|c| = 42.8 \pm 1.5$ nm.

Comparison of this structure to the SAXS data shows a number of similarities. For the level-set model shown in Figure 6c−f, the {111} reflections have the largest structure factor, and their repeat spacing (20.5 ± 0.4 nm) is similar to that of

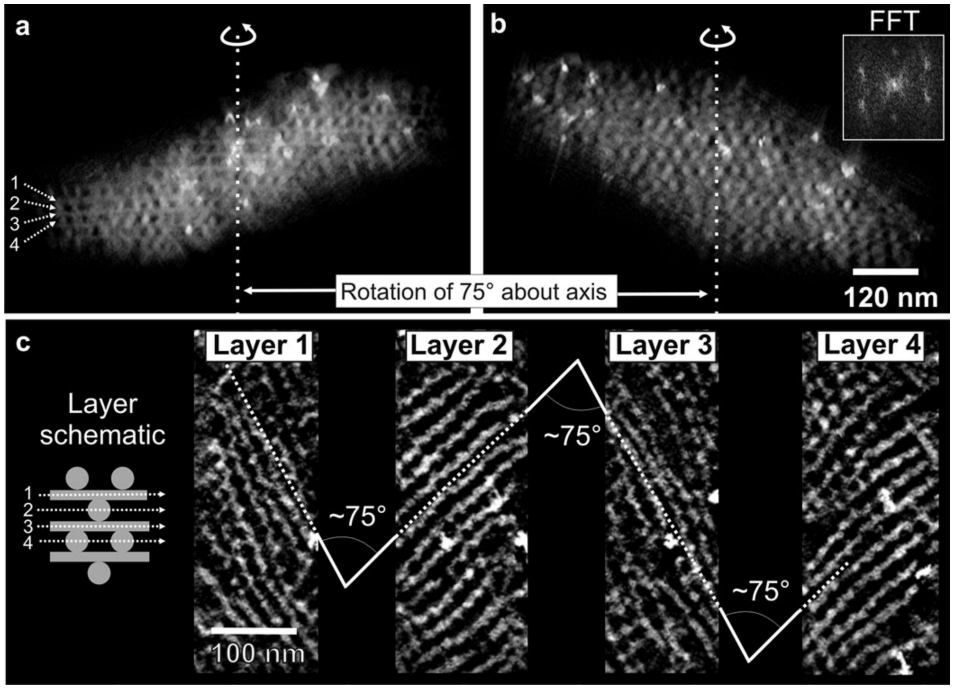

Figure 5. STEM tomographic reconstruction of the bulk specimen (aluminosilicate bright). Voxel projections through volume separated by 75 degrees (a, b). Scale bar is 120 nm in both cases. Inset in (b) shows the 2-D Fourier transform of the density projection. Both projections show layers of strands end-on in a staggered configuration and in addition, strands running across each projection are also just visible. Sections taken through the strand layers at depths of 0, 11, 22, and 33 nm show successive layers of strands running in alternate directions (c). The spacing between strands within each layer is $d_{ip} \approx 23.3$ nm while the angle between the direction of strands in successive layers is $\phi \approx 75°$.

the main ring in the SAXS data (19.4 ± 0.5 nm). Given the bending and twisting of concertinas evident even within the small field of view of the tomographic reconstruction, the absence of higher-order reflections in the SAXS pattern is not surprising. It is difficult to predict the preferred alignment of the structure, but orienting the layers of strands parallel to the film surface (*c*-axis along film normal) is likely to be favorable. For this orientation, the intense {111} reflections should appear at ($|s_x| = 0.043 \pm 0.002$ nm^{-1}, $|s_y| = 0.023 \pm 0.001$ nm^{-1}, 28.6 ± 1.4° from horizontal) which is close to the position of the four bright Bragg spots on the main SAXS ring (Figure 2a). Finally, it should be noted that the scattering features at 22.8 ± 0.5 nm and 17.4 ± 0.5 nm are not consistent with *Fddd* symmetry. The present data are insufficient to determine whether this is because the structure has a lower symmetry, the lattice is skewed, or a small fraction of strands in the sample are packed with a different symmetry.

The woodpile structure is also consistent with TEM images of the isolated domains and bulk material. The process of solvent dispersal used to isolate individual aluminosilicate domains effectively samples a large volume of the material. Examination of a large number of TEM grids of individual aluminosilicate domains showed almost exclusively zigzag, concertina-shaped strands (such as Figure 3b), suggesting this is the predominant domain structure within the material. Furthermore, EF-TEM images of thin sections of the bulk material prepared from different parts of the material all showed the "crossed-strand" motif evident in Figure 3a. This "crossed-strand" motif is inconsistent with parallel strands arranged in a hexagonal or square lattice but is consistent with the woodpile lattice in which strands run in two different directions. Thus, SAXS and TEM microscopy from different regions of the sample are largely consistent with the woodpile structure, although it is important to note that the volume of the tomographic reconstruction shown in Figure 5 is quite small in comparison to the volume of the sample.

Discussion

Two striking features of this material are the zigzag, concertina shape of the aluminosilicate strands and the alternating direction of strands within the woodpile lattice. Rods formed in AB/ABA block copolymers[19] and copolymer/silica materials[53] have a uniform cross section and pack into a parallel, hexagonal array. Thus, the more complicated self-assembly behavior of ABC triblock copolymers is probably responsible for the structure of this material. Previous studies of ABC copolymer systems have reported both strands with nonuniform cross sections[22,43] and strands packed in nonhexagonal (but parallel) arrays.[54,55] However, although examples of the woodpile structure are known at the molecular scale,[28,56,57] it has not been observed in ABC block copolymers.

To better understand this structure, it is important to consider the PEP and PHMA domains surrounding the PEO/aluminosilicate core of each concertina. Because chain stretching is energetically costly,[58] PEP and PHMA chains tend to stretch to the nearest PEO/aluminosilicate domain. Thus, the shape of the polymer sheath is approximately the region of space closest to the core of the concertina[58,59] (a generalized Voronoi cell). Figure 7 shows the generalized Voronoi cell for straight rods arranged in a four-layer woodpile lattice. The region of space closest to the central rod wiggles under the rods in the layer above and over the rods in the layer below, leading to an overall concertina shape. The shape of the Voronoi cell accounts for several aspects of the material's structure.

First, the wiggling of the PEO/aluminosilicate core probably reflects the concertina shape of Voronoi cell. The effect of Voronoi cell shape on inner domain shape has previously been observed in an ABC block copolymer core−shell hexagonal morphology.[60] For straight rods arranged in a woodpile lattice, the surrounding sheath (Figure 7a) is thinnest where rods cross and thickest between rods. These variations in thickness increase the chain stretching energy of the outer PEP and PHMA

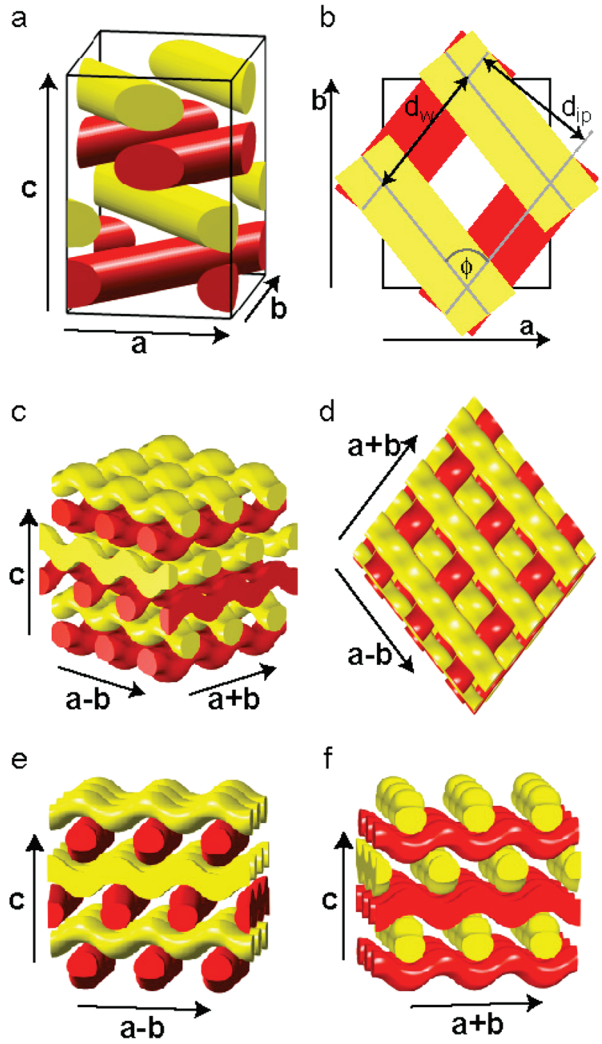

Figure 6. Four-layer woodpile structure. In the face-centered orthorhombic unit cell (side view a**,** top view b), strands in odd/even layers (red/yellow) are directed along the $(\boldsymbol{a} + \boldsymbol{b})/(\boldsymbol{a} - \boldsymbol{b})$ diagonals while the third and fourth layers are offset by $(\boldsymbol{a} + \boldsymbol{c})/2$. The angle between the two strand directions ($\phi \approx 75°$), spacing between strands within each plane (d_{ip}), and period of wiggles along each strand (d_w) are indicated in the overhead view (b). Models of the undulating structure viewed from the front (c), overhead (d), and both strand directions (e, f).

domains. The thickness of the outer sheath becomes more uniform if the core wiggles under the strands in the layer above and over the strands in the layer beneath it, as shown in Figure 8a. Thus, wiggling of the inner domain can lower the chain-stretching energy of the outer domains at the cost of a larger interfacial area. If this mechanism caused the wiggling of the strands, the "zigzag" period of isolated concertinas ($d_w \approx 24$ nm) should match the distance between strand crossings within the woodpile lattice ($d_{ip}/\sin(\phi) \approx 24$ nm), as is indeed the case. Unfortunately, though, the orientation of wiggles along each concertina is not resolved in the tomographic reconstruction.

A second feature of the woodpile lattice is the relative offset of the layers above and below any given layer (Figures 5a,b and 6e,f). Even though these layers are not in direct contact, their relative position affects the shape of the Voronoi cell of the layer of strands sandwiched between them. When the strands in the layers above and below a layer are offset, as in the four-layer woodpile lattice, the variations in Voronoi cell cross section (and chain-stretching energy) are smallest.

Despite the zigzag shape of the PEO/aluminosilicate core, the thickness of the outer polymer layer still varies along its length. If the outer layer consisted of a single component, these variations in chain stretching would be prohibitive when

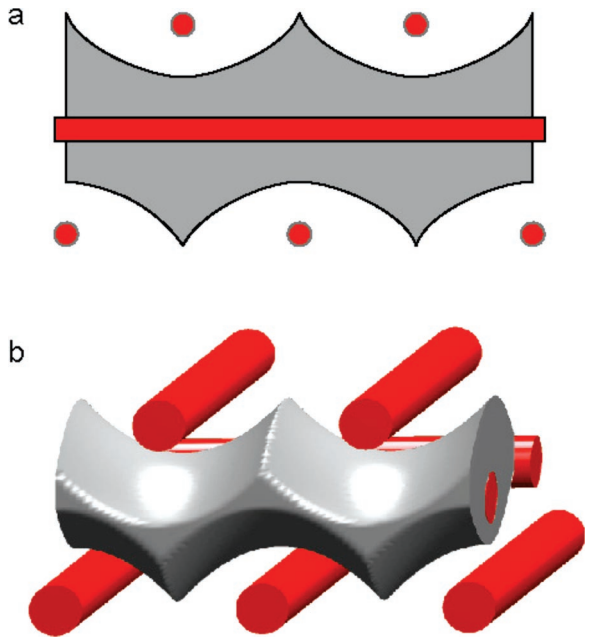

Figure 7. Generalized Voronoi cell for the four-layer woodpile structure. The region of space closest to the central rod is marked in gray in both the two-dimensional section (a) and 3-D view (b). The Voronoi cell wiggles under the rods in the layer above and over the rods in the layer below, leading to a zigzag, concertina shape. The distance from the rod to the cell surface is smallest where strands cross and largest between crossings.

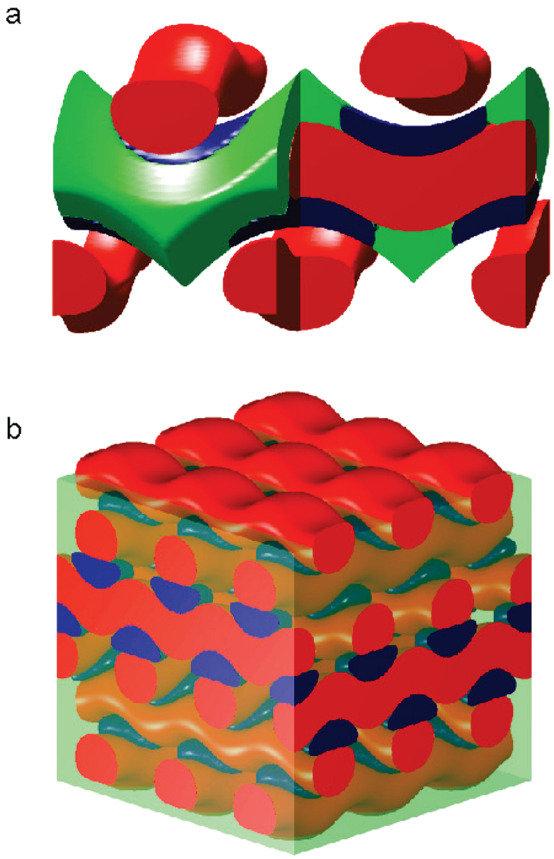

Figure 8. Model distribution of PHMA (green) and PEP domains (blue) surrounding the central PEO/aluminosilicate (red) core of the concertina. The smaller PEP domains are positioned where concertinas cross as shown in both the cutaway view of a single strand (a) and for the full structure (b).

compared to those in the traditional (parallel) hexagonal lattice. However, the optimal thickness of the PEP and PHMA domains on the outside of the concertinas may be different, and the best arrangement of strands should accommodate these differences while also ensuring the PEP and PHMA domains align with those of neighboring strands. Figure 8 shows a plausible arrangement of the PEP (blue) and PHMA (green) domains consistent with the block volume fractions and Voronoi cell shape. The smaller PEP block forms micellar domains bridging the short gaps where concertinas cross. For this model, the optimum distance between concertinas in each layer (d_{ip}) and distance between PEP domains along the top or bottom of the concertina (d_w) determine the angle at which the layers of concertinas cross (ϕ, Figure 6b). This may account for the observed crossing angle of $\phi \sim 75°$ although shrinkage during solvent casting and distortion during microtoming must also be considered.

In structures with a nonparallel packing of rods, the individual rods frequently have a commensurate periodic structure. For example, the helical backbone of γ-isotactic polypropylene[56] is accommodated by an orthorhombic woodpile structure ($\phi \approx 81°$). Similarly, the double-twist tubes in cholesteric blue phases[61,62] cannot pack closely when they are parallel. This general mechanism could also stabilize nonparallel rod morphologies in ABC triblock copolymers, as indicated by the model in Figure 8.

The present work confirms that the complex phase behavior of ABC copolymers provides access to new organic/inorganic material structures. These new structures may be important for applications such as self-assembled photonic band gap materials.[6,63] Although the lattice of the present material is too small for optical wavelengths, the incorporation of inorganic material allows high dielectric contrast within the material[63] and the four-layer woodpile structure has a full three-dimensional photonic band gap,[1,64,65] unlike existing diblock copolymer morphologies.[66]

Conclusion

The morphology of a PEP-*b*-PEO-*b*-PHMA triblock copolymer/aluminosilicate material was determined by scanning transmission electron tomography. In the bulk material, PEO/aluminosilicate strands were arranged in layers with strands in successive layers alternating in direction. This unusual woodpile stacking may be stabilized by a periodic arrangement of PEP and PHMA domains along the outside of each PEO/aluminosilicate strand. The zigzag, concertina shape of the individual strands resembled the shape of the generalized Voronoi cell of the woodpile lattice.

Acknowledgment. We thank Scott Warren for help with synthesis and characterization of polymers and Yuanming Zhang for help in sectioning the hybrid material. This work was supported by the National Science Foundation Grants DMR-0605856, DMR-0404195, DMR-0405195, DMR-0225180 and DMR-0079992 and by Department of Energy BER Grant DE-FG02-97ER62443.

Supporting Information Available: Movie showing the isosurface rendering of the aluminosilicate strand structure obtained from the tomographic reconstruction of an individual hybrid strand, which has a clear "concertina" structure with a wiggle period of ~24 nm (scale bar 25 nm). This material is available free of charge via the Internet at http://pubs.acs.org.

References and Notes

(1) Sozuer, H. S.; Dowling, J. P. *J. Mod. Opt.* **1994**, *41*, 231−239.
(2) Volcani, B. E. In *Silicon and Siliceous Structures in Biological Systems*; Simpson, T. L., Volcani, B. E., Eds.; Springer: New York, 1981; pp 157−200.
(3) Shimizu, K.; Cha, J.; Stucky, G.; Morse, D. E. *Proc. Natl. Acad. Sci. U.S.A.* **1998**, *95*, 6234−6238.
(4) Kroger, N.; Deutzmann, R.; Sumper, M. *Science (Washington, D.C.)* **1999**, *286*, 1129−1132.
(5) Aizenberg, J.; Weaver, J. C.; Thanawala, M. S.; Sundar, V. C.; Morse, D. E.; Fratzl, P. *Science (Washington, D.C.)* **2005**, *309*, 275−278.
(6) Vukusic, P.; Sambles, J. R. *Nature (London)* **2003**, *424*, 852−855.
(7) Schuth, F.; Schmidt, W. *Adv. Mater. (Weinheim, Ger.)* **2002**, *14*, 629−638.
(8) Soler-Illia, G. J. D.; Sanchez, C.; Lebeau, B.; Patarin, J. *Chem. Rev.* **2002**, *102*, 4093−4138.
(9) Kresge, C. T.; Leonowicz, M. E.; Roth, W. J.; Vartuli, J. C.; Beck, J. S. *Nature (London)* **1992**, *359*, 710−712.
(10) Aksay, I. A.; Trau, M.; Manne, S.; Honma, I.; Yao, N.; Zhou, L.; Fenter, P.; Eisenberger, P. M.; Gruner, S. M. *Science (Washington, D.C.)* **1996**, *273*, 892−898.
(11) Tanev, P.; Pinnavaia, T. *Science (Washington, D.C.)* **1996**, *271*, 1267−1269.
(12) Mann, S. *Nature (London)* **1993**, *365*, 499−505.
(13) Yanagisawa, T.; Shimizu, T.; Kuroda, K.; Kato, C. *Bull. Chem. Soc. Jpn.* **1990**, *63*, 1535−1537.
(14) Bagshaw, S. A.; Prouzet, E.; Pinnavaia, T. J. *Science (Washington, D.C.)* **1995**, *269*, 1242−1244.
(15) Antonietti, M.; Goltner, C. *Angew. Chem., Int. Ed. Engl.* **1997**, *36*, 910−928.
(16) Zhao, D. Y.; Feng, J. L.; Huo, Q. S.; Melosh, N.; Fredrickson, G. H.; Chmelka, B. F.; Stucky, G. D. *Science (Washington, D.C.)* **1998**, *279*, 548−552.
(17) Templin, M.; Franck, A.; Du Chesene, A.; Leist, H.; Zhang, Y.; Ulrich, R.; Schadler, V.; Wiesner, U. *Science (Washington, D.C.)* **1997**, *278*, 1795−1798.
(18) Matsushita, Y.; Choshi, H.; Fujimoto, T.; Nagasawa, M. *Macromolecules* **1980**, *13*, 1053−1058.
(19) Bates, F. S.; Fredrickson, G. H. *Phys. Today* **1999**, *52* (Feb), 32−38.
(20) Zheng, W.; Wang, Z. G. *Macromolecules* **1995**, *28*, 7215−7223.
(21) Epps, T. H.; Cochran, E. W.; Bailey, T. S.; Waletzko, R. S.; Hardy, C. M.; Bates, F. S. *Macromolecules* **2004**, *37*, 8325−8341.
(22) Krappe, U.; Stadler, R.; Voigt-Martin, I. *Macromolecules* **1995**, *28*, 4558−4561.
(23) Goldacker, T.; Abetz, V.; Stadler, R.; Erukhimovich, I.; Leibler, L. *Nature (London)* **1999**, *398*, 137−139.
(24) Mahajan, S.; Cho, B. K.; Allgaier, A.; Fetters, L. J.; Coates, G. W.; Wiesner, U. *Macromol. Rapid Commun.* **2004**, *25*, 1889−1894.
(25) Jain, A.; Wiesner, U. *Macromolecules* **2004**, *37*, 5665−5670.
(26) Mahajan, S. Ph.D. Thesis, Cornell University, Ithaca, NY, 2005.
(27) Midgley, P. A.; Weyland, M. *Ultramicroscopy* **2003**, *96* (3−4), 413−431.
(28) O'Keeffe, M.; Andersson, S. *Acta Crystallogr., Sect. A* **1977**, *33*, 914−923.
(29) Bockstaller, M. R.; Mickiewicz, R. A.; Thomas, E. L. *Adv. Mater. (Weinheim, Ger.)* **2005**, *17*, 1331−1349.
(30) Fetters, L. J.; Lohse, D. J.; Richter, D.; Witten, T. A.; Zirkel, A. *Macromolecules* **1994**, *27*, 4639−4647.
(31) Zhu, L.; Cheng, S. Z. D.; Calhoun, B. H.; Ge, Q.; Quirk, R. P.; Thomas, E. L.; Hsiao, B. S.; Yeh, F.; Lotz, B. *Polymer* **2001**, *42*, 5829−5839.
(32) Rogers, S. S.; Mandelkern, L. *J. Phys. Chem.* **1957**, *61*, 985−991.
(33) Hajduk, D. A. Ph.D. Thesis, Princeton University, Princeton, NJ, 1994; pp 45−54.
(34) Tate, M. W.; Eikenberry, E. F.; Barna, S. L.; Wall, M. E.; Lowrance, J. L.; Gruner, S. M. *J. Appl. Crystallogr.* **1995**, *28*, 196−205.
(35) Blanton, T. N.; Huang, T. C.; Toraya, H.; Hubbard, C. R.; Robie, S. B.; Louër, D.; Göbel, H. E.; Will, G.; Gilles, R.; Raftery, T. *Powder Diffr.* **1995**, *10* (2), 91−95.
(36) Vand, V.; Aitken, A.; Campbell, R. K. *Acta Crystallogr.* **1949**, *2*, 398−403.
(37) Radermacher, M. In *Electron Tomography: Three-Dimensional Imaging with the Transmission Electron Microscope*; Frank, J., Ed.; Plenum Press: London, 1992; p 91.
(38) Gilbert, P. *J. Theor. Biol.* **1972**, *36*, 105−117.
(39) Wohlgemuth, M.; Yufa, N.; Hoffman, J.; Thomas, E. *Macromolecules* **2001**, *34*, 6083−6089.
(40) Madkour, T. M. *Chem. Phys.* **2001**, *274*, 187−198.
(41) Schmidt, S. C.; Hillmyer, M. A. *J. Polym. Sci., Part B: Polym. Phys.* **2002**, *40*, 2364−2376.
(42) *Polymer Handbook*, 3rd ed.; Brandrup, J., Immergut, E. H., Eds.; J. Wiley & Sons: New York, 1989; Chapter VII, pp 554−555.
(43) Breiner, U.; Krappe, U.; Abetz, V.; Stadler, R. *Macromol. Chem. Phys.* **1997**, *198*, 1051−1083.

(44) Klotz, M.; Albouy, P.; Ayral, A.; Menager, C.; Grosso, D.; Van der Lee, A.; Cabuil, V.; Babonneau, F.; Guizard, C. *Chem. Mater.* **2000**, *12*, 1721−1728.
(45) Finkenstadt, V. L.; Millane, R. P. *Acta Crystallogr., Sect. A* **1998**, *54*, 240−248.
(46) *Electron Tomography: Three-Dimensional Imaging with the Transmission Electron Microscope*; Frank, J., Eds.; Plenum Press: New York, 1992.
(47) Spontak, R. J.; Fung, J. C.; Braunfeld, M. B.; Sedat, J. W.; Agard, D. A.; Kane, L.; Smith, S. D.; Satkowski, M. M.; Ashraf, A.; Hajduk, D. A.; Gruner, S. M. *Macromolecules* **1996**, *29*, 4494−4507.
(48) Kaneko, T.; Suda, K.; Satoh, K.; Kamigaito, M.; Kato, T.; Ono, T.; Nakamura, E.; Nishi, T.; Jinnai, H. *Macromol. Symp.* **2006**, *242*, 80−86.
(49) Ziese, U.; de Jong, K. P.; Koster, A. *J. Appl. Catal. A* **2004**, *260*, 71−74.
(50) Beiner, M.; Kabisch, O.; Reichl, S.; Huth, H. *J. Non-Cryst. Solids* **2002**, *307*−*310*, 658−666.
(51) Beiner, M.; Huth, H. *Nat. Mater.* **2003**, *2*, 595−599.
(52) *International Tables for Crystallography*; Hahn, Th., Ed.; Kluwer Academic Publishers: Boston 2002; Vol. A, pp 320−321.
(53) Renker, S.; Mahajan, S.; Babski, D. T.; Schnell, I.; Jain, A.; Gutmann, J.; Zhang, Y.; Gruner, S. M.; Spiess, H. W.; Wiesner, U. *Macromol. Chem. Phys.* **2004**, *205*, 1021−1030.
(54) Mogi, Y.; Kotsuji, H.; Kaneko, Y.; Mori, K.; Matsushita, Y.; Noda, I. *Macromolecules* **1992**, *25*, 5408−5411.
(55) Brinkmann, S.; Stadler, R.; Thomas, E. L. *Macromolecules* **1998**, *31*, 6566−6572.
(56) Meille, S. V.; Bruckner, S.; Porzio, W. *Macromolecules* **1990**, *23*, 4114−4121.
(57) Rosi, N. L.; Kim, J.; Eddaoudi, M.; Chen, B.; O'Keeffe, M.; Yaghi, O. M. *J. Am. Chem. Soc.* **2005**, *127*, 1504−1518.
(58) Thomas, E. L.; Kinning, D. J.; Alward, D. B.; Henkee, C. S. *Macromolecules* **1987**, *20*, 2934−2939.
(59) Grason, G. M. *Phys. Rep.* **2006**, *433*, p1−64.
(60) Gido, S. P.; Schwark, D. W.; Thomas, E. L.; Goncalves, M. D. *Macromolecules* **1993**, *26*, 2636−2640.
(61) Wright, D. C.; Mermin, N. D. *Rev. Mod. Phys.* **1989**, *61*, 385−432.
(62) Cao, W. Y.; Munoz, A.; Palffy-Muhoray, P.; Taheri, B. *Nat. Mater.* **2002**, *1*, 111−113.
(63) Yoon, J.; Lee, W.; Thomas, E. L. *MRS Bull.* **2005**, *30*, 721−726.
(64) Ho, K. M.; Chan, C. T.; Soukoulis, C. M.; Biswas, R.; Sigalas, M. *Solid State Commun.* **1994**, *89*, 413−416.
(65) Kopperschmidt, P. *Appl. Phys. B: Laser Opt.* **2003**, *76*, 729−734.
(66) Maldovan, M.; Urbas, A. M.; Yufa, N.; Carter, W. C.; Thomas, E. L. *Phys. Rev. B: Condens. Matter Mater. Phys.* **2002**, *65*, 165123.
(67) Simon, P. F. W.; Ulrich, R.; Spiess, H. W.; Wiesner, U. *Chem. Mater.* **2001**, *13*, 3464−3486.

MA071004S